

High efficiency dark-to-bright exciton conversion in carbon nanotubes

A. Ishii,^{1,2} H. Machiya,^{1,3} and Y. K. Kato^{1,2,*}

¹*Nanoscale Quantum Photonics Laboratory, RIKEN Cluster for Pioneering Research, Saitama 351-0198, Japan*

²*Quantum Optoelectronics Research Team, RIKEN Center for Advanced Photonics, Saitama 351-0198, Japan*

³*Department of Electrical Engineering, The University of Tokyo, Tokyo 113-8656, Japan*

We report that dark excitons can have a large contribution to the emission intensity in carbon nanotubes due to an efficient exciton conversion from a dark state to a bright state. Time-resolved photoluminescence measurements are used to investigate decay dynamics and diffusion properties of excitons, and we obtain intrinsic lifetimes and diffusion lengths of bright excitons as well as diffusion coefficients for both bright and dark excitons. We find that the dark-to-bright transition rates can be considerably high, and that more than half of the dark excitons can be converted into the bright excitons. The state transition rates have a large chirality dependence with a family pattern, and the conversion efficiency is found to be significantly enhanced by adsorbed air molecules on the surface of the nanotubes. Our findings show the nontrivial significance of the dark excitons on the emission kinetics in low dimensional materials, and demonstrate the potential for engineering the dark-to-bright conversion process by using surface interactions.

I. INTRODUCTION

Due to limited screening of the Coulomb interaction, electron-hole pairs form tightly-bound excitons in atomically thin semiconductors such as transition metal dichalcogenides and carbon nanotubes (CNTs) [1, 2]. The stable excitonic states play a central role in the optical processes, leading to unique phenomena such as quantum light emission [3–5], exciton Hall effect [6], and formation of interlayer excitons [7]. In addition, there exist excitonic fine structures within the large binding energy, many of which are dark states with optical transitions forbidden by spin, valley, and parity selection rules [8, 9]. The dark states, although they may seem subtle because of the lack of any spectral signatures, can lead to unexpected optical phenomena and are important for understanding of the exciton physics [10–13].

In particular, the parity-even dark states of excitons in CNTs are known to be responsible for the diminishing emission quantum efficiencies at cryogenic temperatures [14, 15], and various approaches have been taken to circumvent the “dark” nature of these states. For example, same-parity transitions by two-photon excitation [16, 17] and intraexcitonic excitation by terahertz spectroscopy [18, 19] can address the dark states without relying on dipole transitions to and from the ground state, whereas magnetic and electric fields can be used to mix the bright and dark states [20–22]. In the absence of external fields, light emission should not be affected by the presence of dark excitons, and indeed, time-resolved photoluminescence (PL) measurements show that the contribution of the dark excitons to PL intensity is insignificant [23–26].

Here we show that conversion efficiency of the dark excitons to the bright excitons can become higher than 50%, and that a considerable fraction of light emission can originate from the dark states. The kinetics of

the bright and dark excitons in individual air-suspended CNTs are investigated using time-resolved PL measurements, and we determine the effective decay lifetimes and diffusion properties by measuring CNTs with various suspended lengths. We find that the dark excitons have intrinsic lifetimes exceeding our measurement capability, and their decay rates are solely limited by quenching at the tube ends. For long tubes, the dark exciton effective lifetime becomes comparable to the bright-dark transition time, and conversion to the bright excitons occurs efficiently. The transition rates exhibit a large chirality dependence with a family pattern, and we find that it can be significantly enhanced by adsorbed molecules on the CNTs.

II. PHOTOLUMINESCENCE SPECTROSCOPY AND TIME-RESOLVED MEASUREMENTS

Our air-suspended carbon nanotubes are grown over trenches on Si substrates with metal pads, where molecular desorbed states of carbon nanotubes [27] can be observed for an extended period of time [28]. We perform electron-beam lithography and dry etching to form trenches with widths ranging from 0.5 to 4.0 μm . The samples are then oxidized in an annealing furnace at 1050°C for an hour in order to form a 65-nm-thick oxide layer. Another lithography step defines the metal pad areas 50 μm away from the trenches, and sputtering is used to deposit 1.5 nm Ti and 40 nm Pt. Catalyst areas are patterned on the oxide layer near the trenches with a third lithography step, and 0.2-nm thermally evaporated Fe film is deposited and lifted off. Single-walled carbon nanotubes are synthesized by alcohol chemical vapor deposition at 800°C with a growth time of 1 min [29].

PL measurements are performed with a homebuilt sample-scanning confocal microscopy system [29, 30]. We use a wavelength-tunable Ti:sapphire laser where the output can be switched between continuous-wave (CW) and ~ 100 -fs pulses with a repetition rate of 76 MHz. An ex-

* Corresponding author. yuichiro.kato@riken.jp

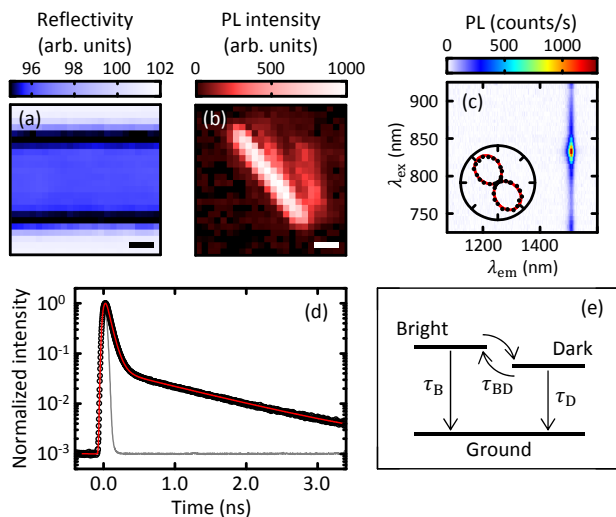


FIG. 1. (a) and (b) Reflectivity and PL images, respectively. $\lambda_{\text{ex}} = 830$ nm and $P = 2 \mu\text{W}$ are used, and the PL image is extracted within a window of 10 nm centered at 1469 nm with integration window. The weaker emission to the right side of the tube is a ghost image arising from excitation laser reflecting at the bottom of the trench. The scale bars are $1 \mu\text{m}$. (c) A PLE map taken with $P = 2 \mu\text{W}$. The inset shows polarization dependence of PL intensity. The red line is a sine fit. (d) PL decay curve measured under pulsed excitation with $\lambda_{\text{ex}} = 825$ nm and $P = 5$ nW. The gray line represents the IRF, and the red curve is the bi-exponential fit. (e) Schematic of the three-level model for exciton decay dynamics.

citation laser beam with power P and wavelength λ_{ex} is focused onto the sample by an objective lens with a numerical aperture of 0.85 and a focal length of 1.8 mm, resulting in a spot size of $\sim 1 \mu\text{m}$. The wavelength-dependent diameter of the focused laser has been characterized by performing PL line scans perpendicular to a suspended CNT. PL and the reflected beam are collected by the same objective lens and separated by a dichroic filter. A Si photodiode detects the reflected beam for imaging, while a translating mirror is used to switch between PL spectroscopy and time-resolved PL measurements. PL spectra are measured with an InGaAs photodiode array attached to a spectrometer, and time-resolved PL measurements are performed using a fiber-coupled superconducting single photon detector and a time-correlated single-photon counting module. The detection wavelength dependent instrument response function (IRF) is obtained by using super-continuum white light pulses dispersed by a spectrometer. All measurements are conducted at room temperature in a nitrogen-purged environment.

For characterizing as-grown suspended CNTs, we perform PL spectroscopy measurements under CW excitation [29]. Line scans along the trenches are used to locate the suspended CNTs, and we take reflectivity and PL images to confirm that they are fully suspended. Figures 1(a) and (b) show reflectivity and PL images, respec-

tively, for a relatively long tube. The PL image at the emission wavelength λ_{em} shows a smooth spatial profile, indicating that the suspended nanotube is defect free and does not contain any quenching sites or trapping sites. Next, we perform PL excitation (PLE) spectroscopy [Fig. 1(c)] to identify the chirality $(n, m) = (11, 7)$ by comparing the E_{11} and E_{22} wavelengths to tabulated data [29]. Polarization dependence of PL intensity is then measured to determine the angle of the nanotube [inset of Fig. 1(c)], and the suspended length $L = 4.8 \mu\text{m}$ is calculated using the angle and the designed trench width.

Using such well-characterized CNTs, we perform time-resolved PL measurements [30] to investigate exciton decay dynamics by mode locking the laser and collecting PL from the center of the nanotube. The excitation laser is tuned to the E_{22} wavelength and the polarization is aligned parallel to the CNT axis unless otherwise noted. Figure 1(d) shows a PL decay curve taken from the same CNT measured in Figs. 1(a-c). The decay curve shows two components with different lifetimes, and a fit is done with a bi-exponential function convoluted with the IRF. The bi-exponential function is defined as $A_1 \exp(-t/\tau_1) + A_2 \exp(-t/\tau_2)$, where t is time and $\tau_1 < \tau_2$, and we obtain the decay lifetimes $\tau_1 = 67$ ps and $\tau_2 = 1216$ ps as well as the intensity fraction of the slow component $Y_2 = A_2\tau_2/(A_1\tau_1 + A_2\tau_2) = 36.6\%$ from the fit. It is surprising that the slow decay component constitutes such a large fraction of the PL intensity, because it is believed to originate from dark excitons converted into bright excitons [23, 24, 26].

The conversion kinetics can be understood by analyzing the bi-exponential decay curve with a three-level model [24], which is schematically shown in Fig. 1(e). The rate equations for the populations of bright excitons N_B and dark excitons N_D are expressed as

$$\frac{dN_B}{dt} = -\left(\frac{1}{\tau_B} + \frac{1}{\tau_{BD}}\right)N_B + \frac{1}{\tau_{BD}}N_D, \quad (1)$$

$$\frac{dN_D}{dt} = -\left(\frac{1}{\tau_D} + \frac{1}{\tau_{BD}}\right)N_D + \frac{1}{\tau_{BD}}N_B, \quad (2)$$

where τ_B and τ_D are the effective decay lifetimes for bright and dark states, respectively, and τ_{BD} is the state-transition time between the bright and the dark states. By solving these kinetic equations assuming an initial population ratio of $N_B : N_D = 1 : 1$, a bi-exponential function representing the time-evolution of N_B can be obtained, which corresponds to the observed PL decay curves. From the experimentally obtained parameters τ_1, τ_2, A_1 , and A_2 , we obtain $\tau_B = 69$ ps and $\tau_D = 2422$ ps as well as $\tau_{BD} = 2369$ ps. The conversion efficiency η_{\uparrow} is given by $\tau_D/(\tau_D + \tau_{BD}) = 51\%$, showing that more than half of the dark excitons are converted to the bright excitons.

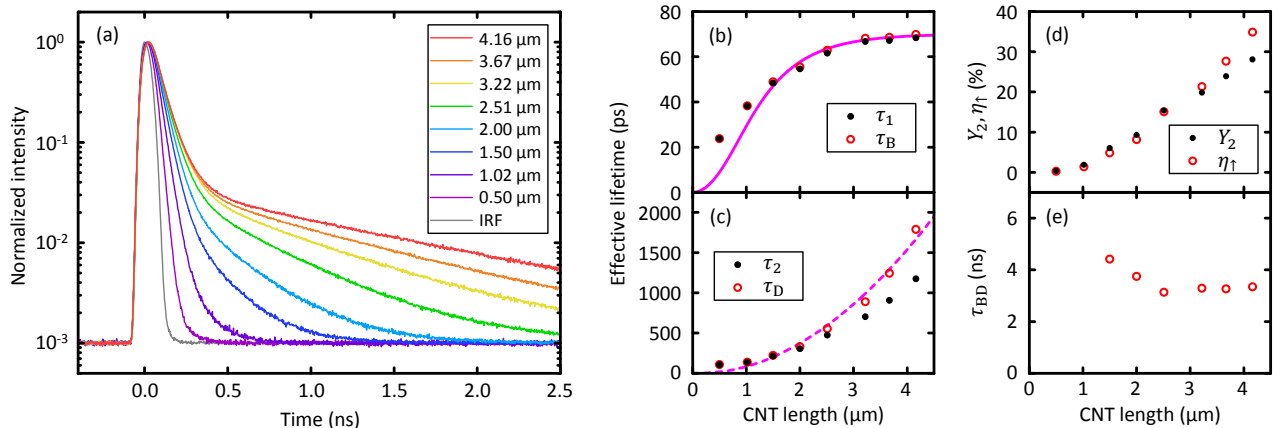


FIG. 2. (a) PL decay curves measured from (9,8) nanotubes with various lengths ranging from 0.5 to 4.2 μm . The gray line is the IRF. $P = 5$ nW and laser polarization parallel to the CNT axis are used. (b) Length dependence of τ_1 (filled circles) and τ_B (open circles). The solid line is the fit with Eq. 4. (c) Length dependence of τ_2 (filled circles) and τ_D (open circles). The broken line is the fit with Eq. 5. (d) Length dependence of Y_2 (filled circles) and η_{\uparrow} (open circles). (e) Length dependence of τ_{BD} . In (b) and (c), data points for $L \leq 1.3$ μm are excluded from the fits.

III. DIFFUSION-LIMITED CONVERSION EFFICIENCY

It turns out that the dark-to-bright conversion efficiency depends strongly on the suspended length. We select (9,8) CNTs with lengths ranging from 0.5 to 4.2 μm and measure PL decay curves with E_{22} excitation at a low power so that the effects of exciton-exciton annihilation can be negligible [29]. The influence of excitation and detection wavelengths as well as the excitation power dependence on the decay dynamics are discussed in the Supplemental Materials [28]. In Fig. 2(a), the PL decay curves taken at various suspended lengths are shown, where drastic changes are observed. As CNT length becomes longer, decay lifetimes of both fast and slow components become longer, and the intensity fraction of the slow component increases. The decay curves are fitted with the bi-exponential function, and the length dependence of τ_1 , τ_2 , and Y_2 are plotted as filled circles in Figs. 2(b-d), respectively. For each CNT, we calculate τ_B , τ_D , η_{\uparrow} , and τ_{BD} as shown by open circles in Figs. 2(b-e), respectively, based on the three-level model. The values of τ_B are very close to τ_1 , while τ_D considerably deviates from τ_2 for long CNTs, indicating that τ_{BD} is important for dark exciton dynamics. Considering the uncertainty of the measurement results for short CNTs where the decay is very fast, τ_{BD} for longer tubes should be considered as the intrinsic values [Fig. 2(e)]. In contrast to τ_B which is almost saturated at CNT lengths longer than 3 μm , τ_D continues to grow even at the longest length, resulting in the steady increase of Y_2 and η_{\uparrow} with the CNT length.

We analyze the length dependence of the effective lifetimes with a random walk theory where the influence of end quenching is evaluated [29, 31]. As the end quenching efficiency depends on the suspended length L and the generated position z of excitons, the effective lifetime is

given by

$$\tau(L) = \frac{\int_{-L/2}^{L/2} g(z) \tau^*(L, z) dz}{\int_{-L/2}^{L/2} g(z) dz}, \quad (3)$$

where $g(z)$ is the normalized Gaussian profile representing the excitation laser profile with a wavelength-dependent spot size. The behavior of $\tau(L)$ is mostly determined by the position-specific lifetime $\tau^*(L, z) = \int_0^{\infty} S_1(t) S_E(L, D, z, t) dt$, where $S_1(t) = \exp(-t/\tau^{\text{int}})$ is the survival probability through intrinsic decay with a lifetime of τ^{int} , and $S_E(L, D, z, t)$ is the end quenching survival probability for excitons generated at z with diffusion coefficient D .

For a finite τ^{int} , we can simplify the expression to [29]

$$\tau^*(L, z) = \tau^{\text{int}} \left\{ 1 - \frac{\cosh(z/l)}{\cosh(L/2l)} \right\}, \quad (4)$$

where $l_B = \sqrt{D\tau^{\text{int}}}$ is the exciton diffusion length, and this model is adopted for the length dependence of τ_B . We obtain the intrinsic lifetime $\tau_B^{\text{int}} = 70$ ps and diffusion length $l_B = 390$ nm as well as $D = 22$ cm^2/s from the fit [solid line in Fig. 2(b)]. The intrinsic lifetime is almost the same as the reported values [26, 32], while the diffusion length is shorter than those reported for similar air-suspended CNTs [29, 33]. We note that this analysis gives the true diffusion length for the bright excitons, while the previously reported values include the dark exciton effects.

For the dark excitons, in contrast, fits by Eq. 4 does not converge because τ_D does not show any sign of saturation, implying that the intrinsic lifetime for dark excitons is much longer than the effective lifetime limited by end

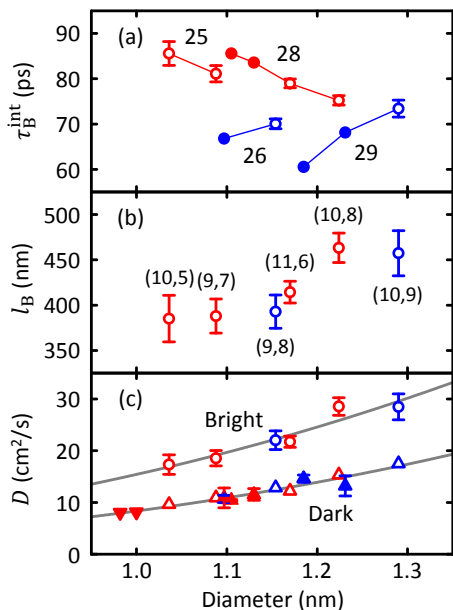


FIG. 3. (a) Diameter dependence of τ_B^{int} . Some more details on data criteria. Open circles are obtained from the length-dependence fit, and filled circles are the longest effective lifetimes measured within the same chiralities. Chiralities with the same family number ($2n+m$) are connected, and the family numbers are displayed. (b) Diameter dependence of l_B . The chiral indices are shown for each data point. (c) Diameter dependence of D for bright excitons (open circles) and dark excitons (triangles). The filled triangles are estimated from a limited number of CNTs, where up and down triangles are obtained from two and one data points, respectively. Gray lines are fit results with a power function. (a-c) Red and blue symbols correspond to type 1 and 2 of chiralities, respectively, and the error bars show the standard error of the fits. Error bars for the open triangles in (c) are not shown as they are smaller than the symbols.

quenching. Letting $\tau_B^{\text{int}} \rightarrow \infty$,

$$\tau^*(L, z) = \frac{L^2 - 4z^2}{8D}, \quad (5)$$

explaining the rapid increase of τ_D with L responsible for the enhanced conversion efficiency. The diffusion coefficient D can be determined by fitting the length dependence [broken line in Fig. 2(c)], and we obtain $D = 13 \text{ cm}^2/\text{s}$.

IV. CHIRALITY DEPENDENCE OF EXCITON DYNAMICS AND THE STATE TRANSITION RATE

We now investigate the chirality dependence of the dark-to-bright conversion efficiency. The same measurements for different chiralities are repeated, and we first characterize the exciton diffusion properties. Figures 3(a) and (b) show τ_B^{int} and l_B , respectively, as a function of

CNT diameter d . Since τ_B is mostly saturated at long CNT lengths [Fig. 2(b)], we also plot the largest values of τ_B for 5 additional chiralities for which multiple CNTs longer than $3 \mu\text{m}$ are measured [filled circles in Fig. 3(a)]. We find a clear family pattern dispersion for τ_B^{int} ranging from 61 ps to 86 ps, whereas l_B shows an increasing trend with the CNT diameter.

The diffusion constant D for the bright excitons is obtained from τ_B^{int} and l_B [open circles in Fig. 3(c)], while D of the dark excitons is directly obtained from the length dependence fits [open triangles in Fig. 3(c)]. In all the chiralities, Eq. 5 accurately reproduces the length dependence of τ_D , indicating that exciton diffusion limits the effective lifetime for the dark excitons. In addition, the fits for the length dependent τ_D can converge with a limited number of data, allowing us to plot D of the dark excitons for 8 additional chiralities [filled triangles in Fig. 3(c)].

The diffusion coefficients for both the bright and dark states show clear diameter d dependence, and we use a power law function $D = D_0(d/d_0)^\alpha$ to fit the data, where D_0 is the diffusion coefficient at the diameter $d_0 = 1 \text{ nm}$ and α is the exponent. The fit results show a good agreement with the experimental data [gray lines in Fig. 3(c)], where we obtain $D_0 = 15.36 \pm 1.24 \text{ cm}^2/\text{s}$ and $\alpha = 2.56 \pm 0.43$ for bright excitons and $D_0 = 8.36 \pm 0.31 \text{ cm}^2/\text{s}$ and $\alpha = 2.79 \pm 0.22$ for dark excitons. The results are consistent with the theoretical prediction of $D \propto d^{2.5}$, where the chirality dependence of the effective mass of excitons and the exciton-phonon scattering rate is considered [34]. We find that D_0 differs by about a factor of 2 between bright and dark excitons, which is reasonable because the effective mass of the bright excitons is much smaller than that of dark excitons due to the difference of their band structures [8]. A quantitative comparison of the theory with the experimental data, however, is still challenging due to other mechanisms of exciton scattering [26].

Finally we discuss the transition rate between the bright and dark states. As we have observed in Fig. 2(e), the transition time τ_{BD} does not depend on CNT length and is more reliable for long CNTs, and therefore we can obtain the intrinsic values from a relatively long CNT for each chirality. In Fig. 4(a), such representative values of τ_{BD} are plotted as a function of CNT diameter, and a clear family pattern on top of a decreasing trend with CNT diameter is observed. It is worth mentioning that such a wide variation of τ_{BD} considerably affects the observed PL decay curves, particularly in the intensity ratio between fast and slow decay components. For example, 2.5- μm -long (12,1) nanotube with $\tau_{BD} = 10.24 \text{ ns}$ shows $Y_2 = 8.6\%$ and $\eta_{\uparrow} = 8.5\%$, while a (10,9) CNT with the same length has $\tau_{BD} = 2.20 \text{ ns}$ exhibiting $Y_2 = 18.2\%$ and $\eta_{\uparrow} = 17.4\%$. The chirality dependence of the bright-dark transition rate is likely related to the bright-dark energy separation ΔE , where a similar family pattern is known with a leading order dependence of $\Delta E \propto 1/d^2$ [35]. To confirm this dependence, we take near-armchair

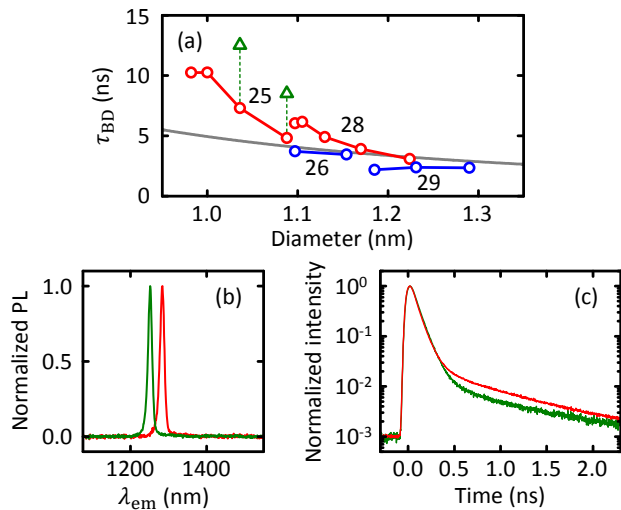


FIG. 4. (a) Diameter dependence of τ_{BD} . The data are taken from tubes with $L \geq 2.5 \mu\text{m}$ and with $P \leq 2 \text{ nW}$. Chiralities with a same family number are connected, and the family numbers are displayed. Red and blue circles correspond to chiralities which belong to type 1 and type 2, respectively. Gray line is a fit described in the text. Green triangles are obtained from molecular desorbed state of (9,7) and (10,5) CNTs. (b) and (c) Normalized PL spectra and PL decay curves, respectively, of a same (9,7) CNT. Red and green lines correspond to molecular adsorbed and desorbed states, respectively.

chiralities from each family group, and a fit is done by assuming $\Delta E = 3 \text{ meV}$ at $d = 1 \text{ nm}$ [20]. The fit result is displayed as a gray line in Fig. 4(a), showing a fairly good agreement with the data.

As the state transition requires a parity flip process, it should be possible to control the conversion efficiency by modifying the exciton scattering site density. We compare the state transition time for a nanotube with and without molecular adsorption [28]. As shown in Fig. 4(b), a blueshift by 32 nm is observed in the PL spectrum of a (9,7) CNT, due to the change of the molecular screening effect [27]. The PL decay curves are taken before and after molecular desorption as shown in Fig. 4(c), and we observe a drastic change of the state transition rate where τ_{BD} increases by a factor of 2, resulting in a decrease of Y_2 and η_{\uparrow} from 16.8% to 9.1% and from 17.3% to 8.7%, respectively. We plot τ_{BD} of the desorbed state for (9,7) and (10,5) CNTs as green triangles in Fig. 4(a). We note that τ_{BD} can be affected by the change of ΔE due to the reduced molecular screening, but it only accounts for 10% of the τ_{BD} reduction if we assume that ΔE scales similar to the E_{11} energy [36]. In addition, we observe

8.9% decrease of τ_D after the molecular desorption. If τ_D is still determined by end quenching as described by Eq. 5, the reduction of τ_D implies 9.7% increase of diffusion coefficient, consistent with the reduced scattering.

V. CONCLUSION

We have investigated exciton dynamics in air-suspended CNTs and have shown that the dark excitons can be converted to the bright state with efficiencies higher than 50%. Time-resolved PL measurements reveal the decay dynamics of excitons, where the bright excitons have intrinsic lifetimes ranging from 61 to 86 ps, while intrinsic lifetimes of the dark excitons are found to be too large to experimentally determine. For long CNTs, the dark exciton decay rate becomes comparable to the bright-dark state transition rate, resulting in a considerable contribution of the dark excitons to the emission intensity. Reflecting the dissimilar lifetimes, the diffusion properties are contrastingly different for bright and dark excitons. By understanding the diffusive motion of the dark states, it should become possible to improve the performance of nanotube single photon emitters as they utilize the mobile nature of excitons [3, 4, 37, 38]. The distinct difference between bright and dark excitons are also expected in other atomically thin materials, which may potentially be used to optimize exciton transport in van der Waals heterostructure photovoltaic devices [39, 40]. We also show chirality dependence of the bright-dark state transition rate, where a wide range of variation with a clear family pattern is observed. Furthermore, by comparing exciton dynamics for pristine and molecular adsorbed states of the same CNTs, we find that the state transition rate is significantly reduced by molecular desorption, suggesting an enhanced parity flip process originating from the adsorbed molecules. If manipulation of multiple exciton species becomes possible by engineering the exciton conversion process, it may lead to development of advanced photonic and optoelectronic devices with devoted channels for exciton transport, recombination, and dissociation.

ACKNOWLEDGMENTS

Work supported by JSPS (KAKENHI JP16K13613 and JP17H07359), MEXT (Nanotechnology Platform), and RIKEN (Incentive Research Project). H.M. acknowledges support by JSPS (Research Fellowship for Young Scientists) and RIKEN (Junior Research Associate Program). We acknowledge the Advanced Manufacturing Support Team at RIKEN for technical assistance.

[1] A. R. Amori, Z. Hou, and T. D. Krauss, Excitons in single-walled carbon nanotubes and their dynamics,

Annu. Rev. Phys. Chem. **69**, 81 (2018).

- [2] T. Mueller and E. Malic, Exciton physics and device application of two-dimensional transition metal dichalcogenide semiconductors, *npj 2D Mater. Appl.* **2**, 29 (2018).
- [3] X. He, N. F. Hartmann, X. Ma, Y. Kim, R. Ihly, J. L. Blackburn, W. Gao, J. Kono, Y. Yomogida, A. Hirano, T. Tanaka, H. Kataura, H. Htoon, and S. K. Doorn, Tunable room-temperature single-photon emission at telecom wavelengths from sp^3 defects in carbon nanotubes, *Nat. Photon.* **11**, 577 (2017).
- [4] A. Ishii, T. Uda, and Y. K. Kato, Room-temperature single-photon emission from micrometer-long air-suspended carbon nanotubes, *Phys. Rev. Applied* **8**, 054039 (2017).
- [5] P. Tonndorf, R. Schmidt, R. Schneider, J. Kern, M. Buscema, G. A. Steele, A. Castellanos-Gomez, H. S. J. van der Zant, S. M. de Vasconcelos, and R. Bratschkitsch, Single-photon emission from localized excitons in an atomically thin semiconductor, *Optica* **2**, 347 (2015).
- [6] M. Onga, Y. Zhang, T. Ideue, and Y. Iwasa, Exciton Hall effect in monolayer MoS_2 , *Nat. Mater.* **16**, 1193 (2017).
- [7] P. Rivera, J. R. Schaibley, A. M. Jones, J. S. Ross, S. Wu, G. Aivazian, P. Klement, K. Seyler, G. Clark, N. J. Ghimire, J. Yan, D. G. Mandrus, W. Yao, and X. Xu, Observation of long-lived interlayer excitons in monolayer MoSe_2 - WSe_2 heterostructures, *Nat. Commun.* **6**, 6242 (2015).
- [8] V. Perebeinos, J. Tersoff, and P. Avouris, Radiative lifetime of excitons in carbon nanotubes, *Nano Lett.* **5**, 2495 (2005).
- [9] E. Malic, M. Selig, M. Feierabend, S. Brem, D. Christiansen, F. Wendler, A. Knorr, and G. Berghäuser, Dark excitons in transition metal dichalcogenides, *Phys. Rev. Materials* **2**, 014002 (2018).
- [10] D. Stich, F. Späth, H. Kraus, A. Sperlich, V. Dyakonov, and T. Hertel, Triplet-triplet exciton dynamics in single-walled carbon nanotubes, *Nat. Photon.* **8**, 139 (2014).
- [11] T. Nishihara, Y. Yamada, M. Okano, and Y. Kanemitsu, Dynamics of the lowest-energy excitons in single-walled carbon nanotubes under resonant and nonresonant optical excitation, *J. Phys. Chem. C* **119**, 28654 (2015).
- [12] X.-X. Zhang, T. Cao, Z. Lu, Y.-C. Lin, F. Zhang, Y. Wang, Z. Li, J. C. Hone, J. A. Robinson, D. Smirnov, S. G. Louie, and T. F. Heinz, Magnetic brightening and control of dark excitons in monolayer WSe_2 , *Nat. Nanotech.* **12**, 883 (2017).
- [13] Y. Zhou, G. Scuri, D. S. Wild, A. A. High, A. Dibos, L. A. Jauregui, C. Shu, K. De Greve, K. Pistunova, A. Y. Joe, T. Taniguchi, K. Watanabe, P. Kim, M. D. Lukin, and H. Park, Probing dark excitons in atomically thin semiconductors via near-field coupling to surface plasmon polaritons, *Nat. Nanotech.* **12**, 856 (2017).
- [14] I. B. Mortimer and R. J. Nicholas, Role of bright and dark excitons in the temperature-dependent photoluminescence of carbon nanotubes, *Phys. Rev. Lett.* **98**, 027404 (2007).
- [15] R. Matsunaga, Y. Miyauchi, K. Matsuda, and Y. Kanemitsu, Symmetry-induced nonequilibrium distributions of bright and dark exciton states in single carbon nanotubes, *Phys. Rev. B* **80**, 115436 (2009).
- [16] F. Wang, G. Dukovic, L. E. Brus, and T. F. Heinz, The optical resonances in carbon nanotubes arise from excitons, *Science* **308**, 838 (2005).
- [17] J. Maultzsch, R. Pomraenke, S. Reich, E. Chang, D. Prezzi, A. Ruini, E. Molinari, M. S. Strano, C. Thom-
sen, and C. Lienau, Exciton binding energies in carbon nanotubes from two-photon photoluminescence, *Phys. Rev. B* **72**, 241402(R) (2005).
- [18] L. Luo, I. Chatzakis, A. Patz, and J. Wang, Ultrafast terahertz probes of interacting dark excitons in chirality-specific semiconducting single-walled carbon nanotubes, *Phys. Rev. Lett.* **114**, 107402 (2015).
- [19] L. Luo, Z. Liu, X. Yang, C. Vaswani, D. Cheng, J.-M. Park, and J. Wang, Anomalous variations of spectral linewidth in internal excitonic quantum transitions of ultrafast resonantly excited single-walled carbon nanotubes, *Phys. Rev. Materials* **3**, 026003 (2019).
- [20] R. Matsunaga, K. Matsuda, and Y. Kanemitsu, Evidence for dark excitons in a single carbon nanotube due to the Aharonov-Bohm effect, *Phys. Rev. Lett.* **101**, 147404 (2008).
- [21] A. Srivastava, H. Htoon, V. I. Klimov, and J. Kono, Direct observation of dark excitons in individual carbon nanotubes: Inhomogeneity in the exchange splitting, *Phys. Rev. Lett.* **101**, 087402 (2008).
- [22] T. Uda, M. Yoshida, A. Ishii, and Y. K. Kato, Electric-field induced activation of dark excitonic states in carbon nanotubes, *Nano Lett.* **16**, 2278 (2016).
- [23] S. Berciaud, L. Cognet, and B. Lounis, Luminescence decay and the absorption cross section of individual single-walled carbon nanotubes, *Phys. Rev. Lett.* **101**, 077402 (2008).
- [24] T. Gokus, L. Cognet, J. G. Duque, M. Pasquali, A. Hartschuh, and B. Lounis, Mono- and biexponential luminescence decays of individual single-walled carbon nanotubes, *J. Phys. Chem. C* **114**, 14025 (2010).
- [25] T. Hertel, S. Himmelein, T. Ackermann, D. Stich, and J. Crochet, Diffusion limited photoluminescence quantum yields in 1-D semiconductors: Single-wall carbon nanotubes, *ACS Nano* **4**, 7161 (2010).
- [26] J. J. Crochet, J. G. Duque, J. H. Werner, B. Lounis, L. Cognet, and S. K. Doorn, Disorder limited exciton transport in colloidal single-wall carbon nanotubes, *Nano Lett.* **12**, 5091 (2012).
- [27] T. Uda, S. Tanaka, and Y. K. Kato, Molecular screening effects on exciton-carrier interactions in suspended carbon nanotubes, *Appl. Phys. Lett.* **113**, 121105 (2018).
- [28] See Supplemental Material for dependences of PL decay dynamics on excitation wavelength, detection wavelength, and excitation power, as well as state transition from molecular desorbed state to adsorbed state.
- [29] A. Ishii, M. Yoshida, and Y. K. Kato, Exciton diffusion, end quenching, and exciton-exciton annihilation in individual air-suspended carbon nanotubes, *Phys. Rev. B* **91**, 125427 (2015).
- [30] A. Ishii, X. He, N. F. Hartmann, H. Machiya, H. Htoon, S. K. Doorn, and Y. K. Kato, Enhanced single-photon emission from carbon-nanotube dopant states coupled to silicon microcavities, *Nano Lett.* **18**, 3873 (2018).
- [31] M. D. Anderson, Y.-F. Xiao, and J. M. Fraser, First-passage theory of exciton population loss in single-walled carbon nanotubes reveals micron-scale intrinsic diffusion lengths, *Phys. Rev. B* **88**, 045420 (2013).
- [32] Y.-F. Xiao, T. Q. Nhan, M. W. B. Wilson, and J. M. Fraser, Saturation of the photoluminescence at few-exciton levels in a single-walled carbon nanotube under ultrafast excitation, *Phys. Rev. Lett.* **104**, 017401 (2010).
- [33] S. Moritsubo, T. Murai, T. Shimada, Y. Murakami, S. Chiashi, S. Maruyama, and Y. K. Kato, Exciton dif-

- fusion in air-suspended single-walled carbon nanotubes, *Phys. Rev. Lett.* **104**, 247402 (2010).
- [34] A. Srivastava and J. Kono, Diffusion-limited exciton-exciton annihilation in single-walled carbon nanotubes: A time-dependent analysis, *Phys. Rev. B* **79**, 205407 (2009).
- [35] R. B. Capaz, C. D. Spataru, S. Ismail-Beigi, and S. G. Louie, Diameter and chirality dependence of exciton properties in carbon nanotubes, *Phys. Rev. B* **74**, 121401(R) (2006).
- [36] J. Lefebvre and P. Finnie, Excited excitonic states in single-walled carbon nanotubes, *Nano Lett.* **8**, 1890 (2008).
- [37] X. Ma, O. Roslyak, J. G. Duque, X. Pang, S. K. Doorn, A. Piryatinski, D. H. Dunlap, and H. Htoon, Influences of exciton diffusion and exciton-exciton annihilation on photon emission statistics of carbon nanotubes, *Phys. Rev. Lett.* **115**, 017401 (2015).
- [38] X. Ma, N. F. Hartmann, J. K. S. Baldwin, S. K. Doorn, and H. Htoon, Room-temperature single-photon generation from solitary dopants of carbon nanotubes, *Nat. Nanotech.* **10**, 671 (2015).
- [39] M. M. Furchi, A. Pospischil, F. Libisch, J. Burgdorfer, and T. Mueller, Photovoltaic effect in an electrically tunable van der Waals heterojunction, *Nano Lett.* **14**, 4785 (2014).
- [40] S. Memaran, N. R. Pradhan, Z. Lu, D. Rhodes, J. Ludwig, Q. Zhou, O. Ogunsolu, P. M. Ajayan, D. Smirnov, A. I. Fernandez-Dominguez, F. J. Garcia-Vidal, and L. Balicas, Pronounced photovoltaic response from multilayered transition-metal dichalcogenides PN-junctions, *Nano Lett.* **15**, 7532 (2015).